Inducing in situ, nonlinear soil response applying an active source

Paul A. Johnson,[1] Paul Bodin,[2] Joan Gomberg,[3] Fred Pearce,[4] Zack Lawrence,[5] and Farn-Yuh Menq[6]

[1]   It is well known that soil sites have a profound effect on ground motion during large earthquakes. The complex structure of soil deposits and the highly nonlinear constitutive behavior of soils largely control nonlinear site response at soil sites. Measurements of nonlinear soil response under natural conditions are critical to advancing our understanding of soil behavior during earthquakes. Many factors limit the use of earthquake observations to estimate nonlinear site response such that quantitative characterization of nonlinear behavior relies almost exclusively on laboratory experiments and modeling of wave propagation. Here we introduce a new method for in situ characterization of the nonlinear behavior of a natural soil formation using measurements obtained immediately adjacent to a large vibrator source. To our knowledge, we are the first group to propose and test such an approach. Employing a large, surface vibrator as a source, we measure the nonlinear behavior of the soil by incrementally increasing the source amplitude over a range of frequencies and monitoring changes in the output spectra. We apply a homodyne algorithm for measuring spectral amplitudes, which provides robust signal-to-noise ratios at the frequencies of interest. Spectral ratios are computed between the receivers and the source as well as receiver pairs located in an array adjacent to the source, providing the means to separate source and near-source nonlinearity from pervasive nonlinearity in the soil column. We find clear evidence of nonlinearity in significant decreases in the frequency of peak spectral ratios, corresponding to material softening with amplitude, observed across the array as the source amplitude is increased. The observed peak shifts are consistent with laboratory measurements of soil nonlinearity. Our results provide constraints for future numerical modeling studies of strong ground motion during earthquakes.

1. Introduction

[2]   As many populated areas and infrastructure are located on soils, particular emphasis has been placed on predicting earthquake ground motion at soil sites. The term "site response" is often used to describe the influence of local site conditions on earthquake ground motion. Soils have low wave speeds relative to rocks because of their unconsolidated, granular microstructure, which leads to locally amplified earthquake ground motions. In addition, the layered structure of soil deposits often contains strong impedance contrasts, such as the soil-rock interface or the water table, which traps seismic energy near the surface. In this case, reverberations within soil layers further amplify ground motion at one or more resonance frequencies of the soil formation [*Williams et al.*, 2000]. When large ground motion is expected, nonlinear soil behavior must be addressed to accurately predict site response for soil sites. Soil nonlinearity originates at the microscale from interactions between soil grains, and has been extensively studied through laboratory experiments [*Hardin*, 1972; *Seed et al.*, 1986; *Stokoe et al.*, 2001; *Loukachev et al.*, 2002; *Johnson and Jia*, 2005; *Brunet et al.*, 2008]. Such experiments have shown that soil microstructure begins to "soften" when dynamic strains exceed about 10^{-6} at ambient pressure conditions whereby the soil dynamic modulus and quality factor (Q) decrease in proportion to amplitude [*Hardin*, 1972; *Johnson and Jia*, 2005]. Furthermore, laboratory measurements have shown the amplitude dependence of soil modulus and Q within the large-strain regime is strongly dependent on confining pressure, grain size, and water content [e.g., *Hardin*, 1972; *Johnson and Jia*, 2005; *Van Den Abeele et al.*, 2002; *Zinszner et al.*, 1997], which

[1]Geophysics Group, Los Alamos National Laboratory, Los Alamos, New Mexico, USA.
[2]Department of Earth and Space Sciences, University of Washington, Seattle, Washington, USA.
[3]U.S. Geological Survey, Department of Earth and Space Sciences, University of Washington, Seattle, Washington, USA.
[4]Earth Resources Laboratory, MIT, Boston, Massachusetts, USA.
[5]ExxonMobil Upstream Research Company, Houston, Texas, USA.
[6]Geotechnical Engineering Center, Department of Civil, Architectural and Environmental Engineering, University of Texas at Austin, Austin, Texas, USA.

Table 1. Geophysical Properties of the Upper 4.27 m[a]

	Water Content (%)	Degree of Saturation (%)	Void Ratio	Fines Content (%)	Total Unit Weight[b] (pcf)	Dry Unit Weight[b] (pcf)
1.71	8	NA	NA	61–65	NA	NA
1.83	16	89	0.5	61–65	131.1	131.0
2.13	NA	NA	NA	61–65	112.3	NA
2.56	22	81	0.7	82–84	118.3	97.1
2.68	25	75	0.9	82–84	110.7	88.6
2.80	24	93	0.7		122.7	99.1
3.23	18	57	0.8	80–83	107.3	90.9
3.38	8	24	0.9	80–83	96.1	89.1
3.54	10	31	0.8		99.7	90.7

[a]Properties listed are from *Kurtulus et al.* [2005, Table 3], measured on undisturbed samples (see *Kurtulus et al.* [2005] for details). Lab tests of disturbed samples from the top 4.27 m show that over this depth range the soil is composed of nonplastic silt with ~0.46 m thick silty sand layers at the top and bottom of the profile. Specific gravity of 2.68 is assumed. NA, not available.

[b]Here pcf, pounds per cubic foot.

can vary greatly in natural soil deposits. Currently, there is a near complete reliance on laboratory experiments to quantify the nonlinear behavior of soils for site response prediction [*Stokoe et al.*, 2001]. However, laboratory experiments cannot necessarily replicate in situ material state, including impedance contrasts and boundary conditions.

[3] One of the first definitive observations of nonlinear site response induced by a large earthquake was obtained from the 1994 M6.7 Northridge, California earthquake [*Field et al.*, 1997, 1998]. In that study, computed spectral ratios between many soil and rock sites, a measure of site response, revealed a systematic decrease in the frequency of main shock peak spectral ratios compared to those for aftershocks. Field et al. concluded that the observed decrease in peak frequency across the Los Angeles Basin resulted from nonlinear soil behavior. In addition, a decrease in the peak amplitude of the spectral ratios for the main shock was also observed, indicating an overall decrease in Q during the main shock. Subsequent observations from large earthquakes have shown additional evidence for nonlinear site response at soil sites [e.g., *Holzer et al.*, 1989; *Beresnev and Wen*, 1996; *Satoh et al.*, 1995, 2001; *Bonilla et al.*, 2005; *Holzer and Youd*, 2007].

[4] Local, nonlinear site response is very difficult to extract from measurements of earthquake ground motion, which should not be surprising given the uncertainties in the motions expected in the absence of nonlinear response. Models of motions expected at a site unaffected by nonlinearity depend on details of the source magnitude, spectral characteristics and radiation, and seismic wave propagation to the site. The ground motion model parameters for any earthquake are generally inferred from observations at relatively sparsely distributed (km or more) recording stations (usually presumed to be unaffected by nonlinearity). A measurable nonlinear response requires an earthquake with sufficient magnitude and/or sufficiently close proximity to a recording station to generate large-amplitude ground motion. Earthquake site response studies often employ a nearby reference site in rock to remove source and path effects. The choice of reference site can significantly influence site response estimates [*Steidl et al.*, 1996; *Bonilla et al.*, 2002], particularly if nonlinearity is present [*Bonilla et al.*, 2005]. Furthermore, aftershocks are frequently used

as a reference to infer relative changes in spectral ratios associated with nonlinearity [e.g., *Field et al.*, 1997]. However, time-dependent effects observed during large earthquakes [*Pavlenko and Irikura*, 2003; *Lawrence et al.*, 2008] and in laboratory experiments on granular materials [e.g., *Johnson and Jia*, 2005; *Brunet et al.*, 2008] may potentially contaminate the aftershock spectral ratios because the soil structure may take several days to recover after the main shock. The recovery process is known as slow dynamics in laboratory studies on granular media and rock [e.g., *Johnson and Jia*, 2005; *Guyer and Johnson*, 1999; *Johnson et al.*, 1996; *Johnson and Sutin*, 2005; *TenCate and Shankland*, 1996]. While earthquake observations have documented the general character of nonlinear soil response, no current approach exists for actively measuring the in situ nonlinear behavior of a natural soil deposit.

[5] In this paper, we describe a new method for characterizing the nonlinear behavior of a natural soil formation using an active source. A large vibrator truck is used to generate a steady state wavefield in the soil formation across a broad range of frequencies and amplitudes. We collect measurements of the source output and three components of ground motion within a small array immediately adjacent to the source. The same vibrator truck was used in experiments described by *Lawrence et al.* [2008]. In that work experiments were conducted at a different location and the analysis was focused on measurements of surface wave dispersion. Here we measure nonlinear soil behavior by examining changes in steady state spectral ratios between receiver pairs as the source amplitude is increased. We employ a novel application of a homodyne algorithm to deal with data inconsistencies and to maximize the signal-to-noise ratio, a method widely applied to RF waves as well as for low-noise detection of continuous acoustical waves in the laboratory. The homodyne method relies on multiplying a reference wave signal at a given frequency with the detected signal at the same frequency. It is an effective method for eliminating noise. Use of this type of method is essential for minimizing the contamination from harmonics generated by source nonlinearity, which can be significant for vibrator truck sources [e.g., *Lebedev and Beresnev*, 2004]. We consider several types of spectral ratios to help separate nonlinearity of the soil formation from source and near-source effects such as those documented by *Lebedev and Beresnev* [2004].

[6] We focus this study on the development of new experimental and data analysis procedures for measuring nonlinear soil behavior. We first describe the site and instrumentation used in the experiment, then the experimental protocol followed by analysis method and the description of the homodyne method. This is followed by the results, discussion and conclusions.

2. Experiment

2.1. Site Description

[7] We conducted our experiment at the Capitol Aggregates Test site near Austin, Texas where 11 m of young, unconsolidated point bar sediments overlie a soft shale (point bars are deposits formed along the inside of a river bend). The site was selected primarily because of extensive
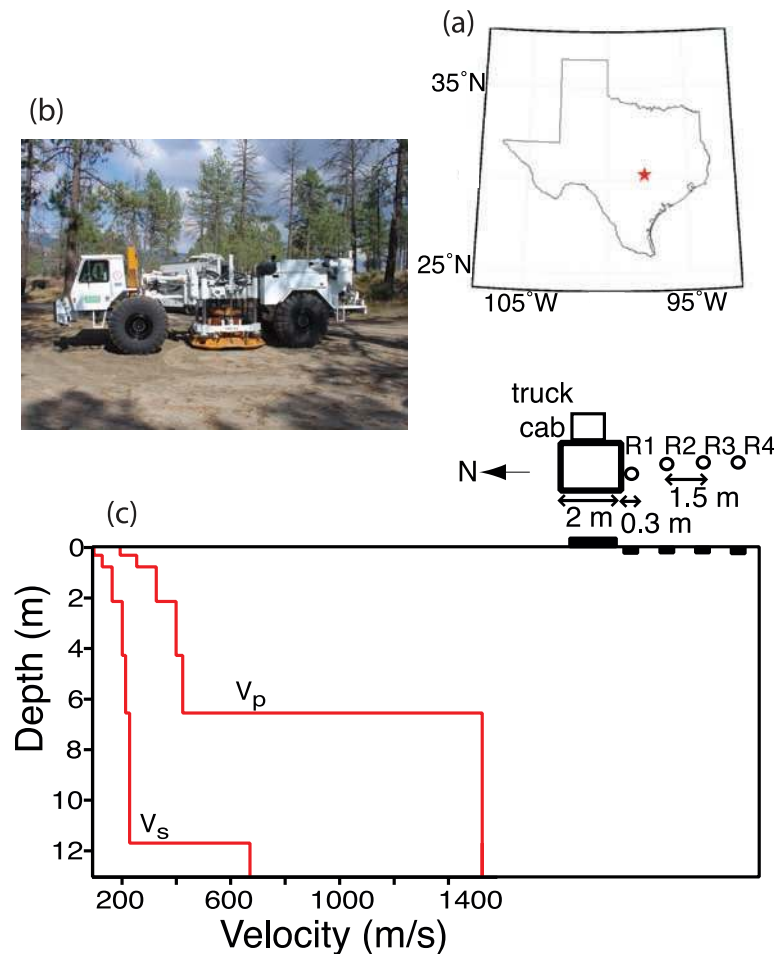
Figure 1. Field site description. (a) The red star on the Texas map indicates the field site in the city of Austin. (b) The experimental layout with the location of the vibrator truck. Source (square) and recording sites (open circles, R1–R4). (c) Velocity profiles measured by *Kurtulus et al.* [2005] for shear waves (*Vs*) and compressional waves (*Vp*).

site characterization work previously conducted by *Kurtulus et al.* [2005]. Near-surface soils consist of predominately nonplastic silt with intermittent silty sand, on the basis of borehole soil samples. We list soil properties measured from these undisturbed samples (Table 1), taken from *Kurtulus et al.* [2005, Tables 2 and 3]. Results from the Spectral Analysis of Surface Waves (SASW) method provided a shear velocity profile [*Kurtulus et al.*, 2005], which we supplemented with a shallow refraction survey to constrain near surface *P* wave velocity (Figure 1 and Table 2). The resulting velocity profile shows a sharp increase in wave speeds with increasing depth and significant impedance contrasts (interfaces between layers) at depths of about 2 m, 4.5 m, 7 m (water table) and 11 m (shale "bedrock"). Complex resonances would be expected in such a soil column. Moreover, dynamic laboratory testing of samples from the site show the soils behave nonlinearly when subjected to large strains, and in manners consistent with generalized models of these types of sediments [*Seed et al.*, 1986; *Darendeli*, 2001; *Johnson and Jia*, 2005]. For example, *Kurtulus et al.* [2005] performed tests on samples from 1.8-m and 2.8-m depth in a combined resonant column and torsional shear device at confining pressures of 41.4 kPa and

165.5 kPa and measure "elastic threshold" and "reference" strains of 7 to 14 microstrains and 400 to 900 microstrains, respectively. The elastic threshold is the value above which the shear modulus depends on the strain amplitude and the reference strain is the value at which the shear modulus has decreased by half its low-strain elastic value.

2.2. Instrumentation

[8] We used a large vibrator truck, called "T-Rex," developed and maintained as part of the Network for

Table 2. Site Compressional and Shear Wave Velocity Profile[a]

Depth to Top of Layer (m)	Compressional Wave Velocity (m/s)	Shear Wave Velocity (m/s)	Poisson's Ratio
0	193.5	97.54	0.33
0.305	254.2	128	0.33
0.762	326.7	164.6	0.33
2.13	399.3	201.2	0.33
4.27	423.7	213.4	0.33
6.55	1524	228.6	0.49
11.7	1524	670.6	0.38

[a]From *Kurtulus et al.* [2005, Table 6]. Best fitting velocity profiles estimated from an SASW analysis at the site.
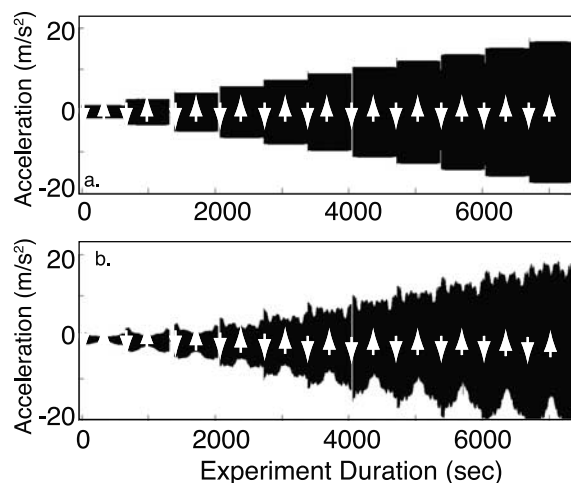
Figure 2. Unfiltered time signals for one entire experiment recorded (a) directly from the function generator and (b) at the source-ground contact. Down arrows denote down sweep start times, and up arrows mark switches from down sweeps to upsweeps. Each step sweep lasts approximately 325 s.

Earthquake Engineering Simulation Program of the National Science Foundation (K. H. Stokoe et al., Development of the NEES large-scale mobile shakers and associated instrumentation for in situ evaluation of nonlinear characteristics and liquefaction resistance of soils, paper 535 presented at 13th World Conference on Earthquake Engineering, Can. Assoc. for Earthquake Eng., Vancouver, B. C., Canada, 2004). The T-Rex has a maximum vertical force output of approximately 267 kN (27.2 t). The source couples to the ground via a 2 × 2 m^2 plate and is capable of shaking over a broad frequency band (~10–180 Hz). A function generator controls the frequency and amplitude of the source while accelerometers built into the truck estimate the resulting force output to the ground. The input function generator signals and the corresponding force output (that exerted by the pad onto the ground) are recorded for analysis. The latter force is derived from the signal recorded by the accelerometer mounted on the mass, the mass of the entire system, and forcing from the hydraulic driving system. The T-Rex can vibrate vertically and horizontally; in this prototype study we consider only vertical shaking.

[9] The near-source wavefield was recorded using four receivers, R1–R4, with increasing distance from the source as shown in Figure 1. The closest receiver was 0.35 m from the edge of the source plate, and receivers spaced 1.5 m from one another. The vertical component accelerometer on the source plate was mounted in the southwest corner of the plate, the closest corner to the first receiver. The receivers were Kinemetrics three-component accelerometers designed for large accelerations (>2g). Our array extends along a N–S line from the source; therefore, we consider only the vertical (Z) and radial (N–S) components of acceleration, which will be the dominant directions of ground motion. Each receiver was anchored to a concrete pad with diameter of approximately 0.35 m (much smaller than wavelengths). The concrete pads were designed to match the soil density and each pad was of equal dimension within a few centimeters. All recorded time signals (source and receivers) have a time sampling of 0.005 s and are converted to SI units of acceleration (m/s/s) using the nominal instrument sensitivities.

2.3. Experimental Protocol

[10] Unlike measurements using earthquake-generated waves, we measure the soil response at discrete frequencies within a limited band following a methodology employed in the laboratory known as Nonlinear Resonance Ultrasound Spectroscopy (NRUS) [e.g., *Johnson et al.*, 1996; *Johnson*, 1999]. The source protocol is composed of an up and down step sweep. We will show several complete upsweeps and down sweeps in Figures 2 and 3, but our analysis is focused only on the down sweeps. For the down sweeps, the source is stepped through $M = 201$ discrete frequencies beginning at 50 Hz (f_1) and decreasing with frequency step size of 0.2 Hz (df) as follows:

$$f_m = f_1 - (m - 1) \, df, m = 1, \ldots, M. \qquad (1)$$

The down sweep decreases in frequency as a function of time to a minimum frequency $f_{min} = 10$ Hz. The source was held at each frequency for 40 cycles to be certain steady state conditions were reached. We repeat the down sweep for $N = 11$ source amplitudes beginning at an input voltage of 0.2 V (A_1) with a step size of 0.2 V (dA) as follows:

$$A_n = A_1 + (n - 1) \, dA, n = 1, \ldots, N. \qquad (2)$$

On the basis of this source protocol, we obtain acceleration time series for the source and receivers, which contain the steady state system response at each step sweep frequency f_m and each source amplitude A_n.

3. Envelope Analysis and Harmonic Contamination

[11] In this section we present the data from our experiment and describe significant characteristics. Figure 2 shows a comparison between the input vertical acceleration obtained from the function generator (Figure 2a) and the vertical acceleration measured on the vibrator truck (Figure 2b) for one entire experiment, including all frequencies f_m at all amplitude levels A_n. Both down sweeps and upsweeps (frequencies step from high to low and then low to high, respectively) are conducted and are shown. We discuss only down sweeps. Figure 2b shows that the vibrator truck produces variable amplitudes across the step sweep band, particularly at low frequencies (<15 Hz).

[12] Figure 3 shows the vertical (left) and N–S (right) recorded accelerations at the four receiver sites. We observe a clear difference between the receiver array acceleration time signals and the measured acceleration time signal at the source (Figure 2). As expected, the receiver signals have smaller peak amplitudes than those for the measured source acceleration because of both linear and nonlinear soil dissipation. Both components have more pronounced spikes in amplitude when compared to the measured source acceleration, particularly the N–S component. For the vertical component, there is a slight decrease in amplitude with distance from the source; however, the N–S amplitudes are largest at receivers R2 and R3.
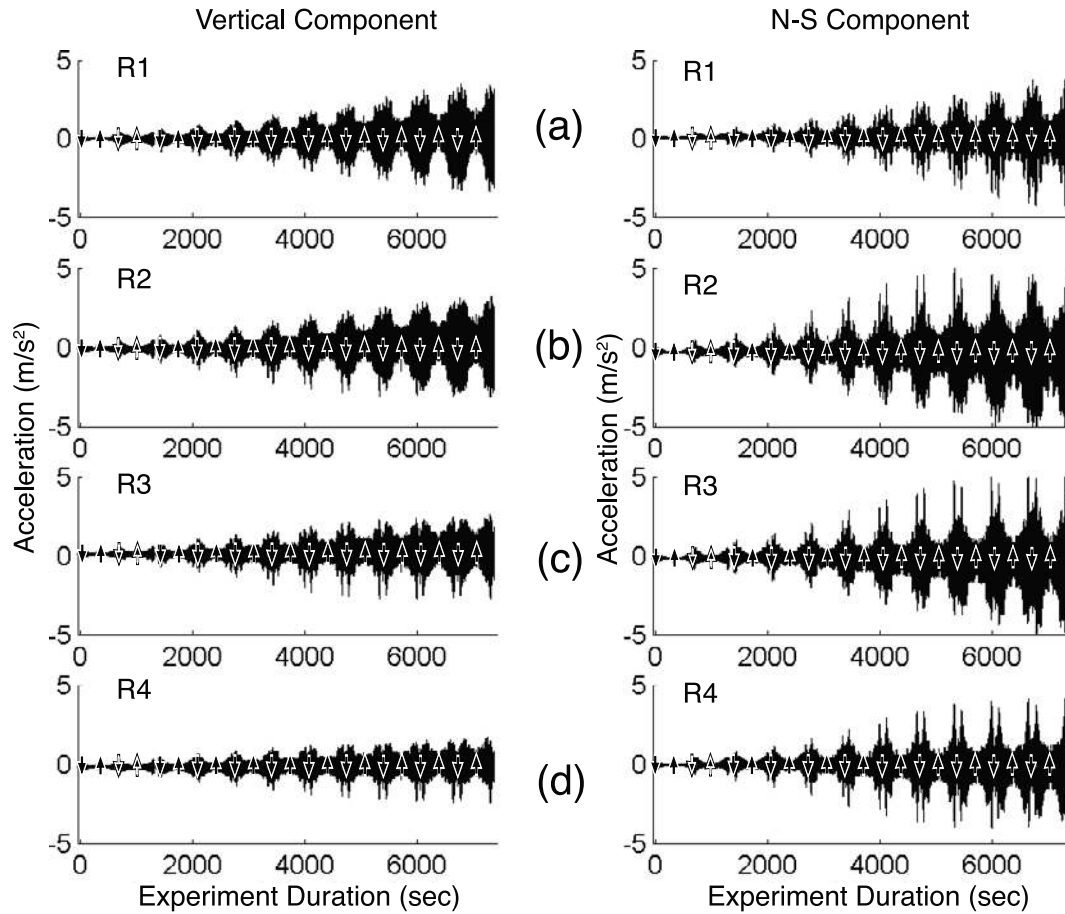
Figure 3. Unfiltered time signals for (left) vertical component and (right) N−S component recorded at (a) R1, (b) R2, (c) R3, and (d) R4. Notation is same as Figure 2.

[13] We see that the receiver signals are generally more complex than the measured source output. Vibrator trucks are well known to generate significant harmonic amplitudes, particularly at their low-frequency limit where coupling becomes inefficient [e.g., *Lebedev et al.*, 2006]. On the basis of the time signals alone, we have no way of distinguishing between the harmonics generated by the source and the material. To gain insight into the relative contribution of harmonics, we consider an analytic signal representation of our experimental data. The analytic representation refers to a complex signal (X_A) in which the real part is the original experimental data (X_D) and the imaginary part is the 90° phase shifted version of the original data obtained from the Hilbert transform (X_H)

$$X_A(t) = X_D(t) + iX_H(t). \tag{3}$$

The magnitude of the analytic signal is defined as the envelope (E),

$$E(t) = \sqrt{\left[X_D(t)^2 + X_H(t)^2\right]} \tag{4}$$

and the phase angle of the analytic signal is defined as the instantaneous phase (φ)

$$\phi(t) = \tan^{-1}\left(\frac{X_H(t)}{X_D(t)}\right), \tag{5}$$

where $\tan^{-1}()$ is the four quadrant inverse tangent function. In the case of step sweeps, it is instructive to consider the instantaneous frequency (Ω) obtained from the first time derivate of the unwrapped, instantaneous phase

$$\Omega(t) = \frac{d\Phi^u(t)}{2\pi dt}, \tag{6}$$

where the superscript u denotes the unwrapped phase and 2π converts radians to Hz.

[14] Figure 4a shows the instantaneous frequency and amplitude envelope for unfiltered down sweeps from the function generator (dashed curves) and the measured baseplate source output (solid curves). The scatter about the dashed line in the top of Figure 4a is a direct measure of the harmonics (including subharmonics) generated by wave distortion at the baseplate. Moreover, the highest-amplitude
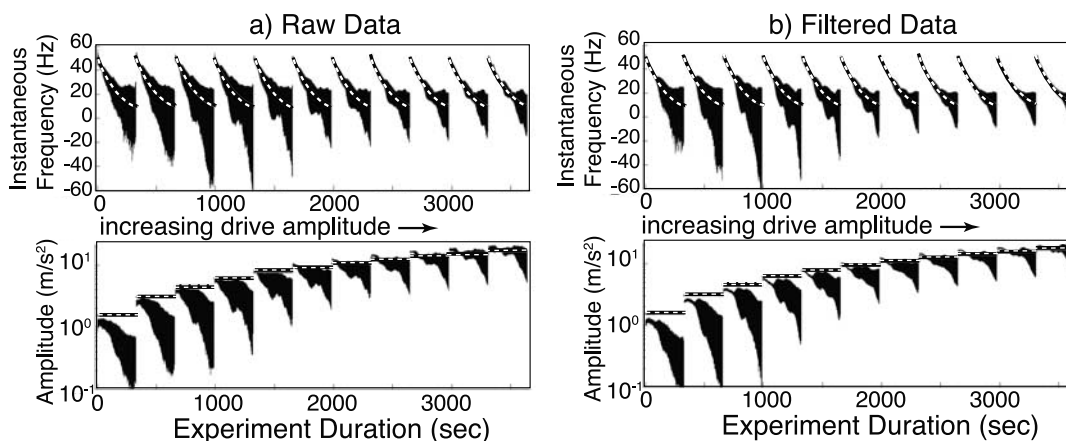
Figure 4. Instantaneous frequency and amplitude envelope of unfiltered time signals from input function generator (dashed) and measured source-ground contact (solid) plotted as a function of time for each down sweep, each corresponding to an increased source amplitude (from left to right). The source amplitude was increased 11 times as the experiment progressed. Results plotted are for data (a) unfiltered and (b) band-pass-filtered from 10 Hz to 50 Hz. Note that the function generator results in Figure 4b have also been filtered to verify filter response.

sweeps show the least wave distortion at the baseplate. Likewise, the amplitude envelopes illustrate the huge variation of amplitude during a sweep, and how poor the amplitude control is for the low-amplitude sweeps. Like the frequency, the amplitude is better behaved at large drive level. (Note that the antialiasing filter is approximately 90 Hz.) In summary, the scatter in the instantaneous frequency and amplitude envelopes of the measured source output provides a relative measure of the harmonic distortion generated by the source, and shows the truck is more nonlinear at lower drive levels because of poor coupling. Moreover, the homodyne analysis described below indicates that the truck hydraulic control does not function well below about 20 Hz. Filtering the time signals to include only frequency components within the down sweep band (10–50 Hz) only slightly reduces the observed scatter (Figure 4b), implying that most of the frequency distortion takes place within the band of interest. This fact makes processing and therefore interpretation difficult. The overlap between harmonics and fundamental frequencies must be addressed when designing an analysis method to extract the amplitude of each fundamental frequency in the step sweep. In addition, the time duration of each step in the step sweep was not constant. Thus determining the beginning and end of a frequency step was challenging. We applied a homodyne analysis to address these issues.

4. Homodyne Analysis

[15] In this section, we first describe the homodyne analysis used to extract the steady state amplitude at each frequency in the step sweep. On the basis of this analysis, we construct a steady state amplitude spectrum for every time signal recorded during our experiment. We provide details about the homodyne analysis in the Appendix.

4.1. Homodyne

[16] We use a homodyne, which we will describe as it applies to a single acceleration time signal recording a down sweep. Homodynes maximize signal-to-noise ratio at a

selected frequency and are used for extracting a signal frequency of interest in many different areas of electronics, physics and acoustics. In acoustical studies for instance, lock-in amplifiers employ a homodyne (or a similar idea known as a heterodyne) to detect continuous waves that may be masked by other signals at different frequencies. Homodyne detection is a method of detecting frequency-modulated waves (a wave containing harmonics for example) by electrical mixing (multiplying) a reference frequency wave with a detected signal.

[17] The idea underlying the method is illustrated by considering the product of a sinusoidal reference signal, $\cos(\omega_r t)$, at the frequency of interest, f_r (with corresponding angular frequency $\omega_r = 2\pi f_r$) and the detected signal, $u(t)$, that may contain N frequency components, i.e., $u(t) = \sum_{n=1}^{N} A(\omega_n)\cos(\omega_n t)$. We wish to measure the amplitude of the frequency component of $u(t)$ corresponding to the frequency of interest ω_r. For simplicity here we ignore any constant phase shifts (see the Appendix for a complete derivation), and find the product of the reference and detected signals is proportional to

$$u(t)\cos(\omega_r t) = \frac{1}{2}\sum_{n=1}^{N} A(\omega_n)\{\cos[(\omega_n - \omega_r)t] + \cos[(\omega_n + \omega_r)t]\}.$$

(7)

When the output signal frequency component equals the reference frequency, the first term of this cosine sum becomes the zero frequency component with amplitude equal to $A(\omega_t)$, which may be extracted by low-pass filtering, or other means. This is the essence of the homodyne. In reality, the reference signal is composed of an in-phase and quadrature component in order to obtain the true amplitude.

[18] The homodyne procedure is normally accomplished using a frequency multiplier mixer in real time, for instance in a lock-in amplifier. We devised a method to create the homodyne in post processing. To our knowledge, this is the
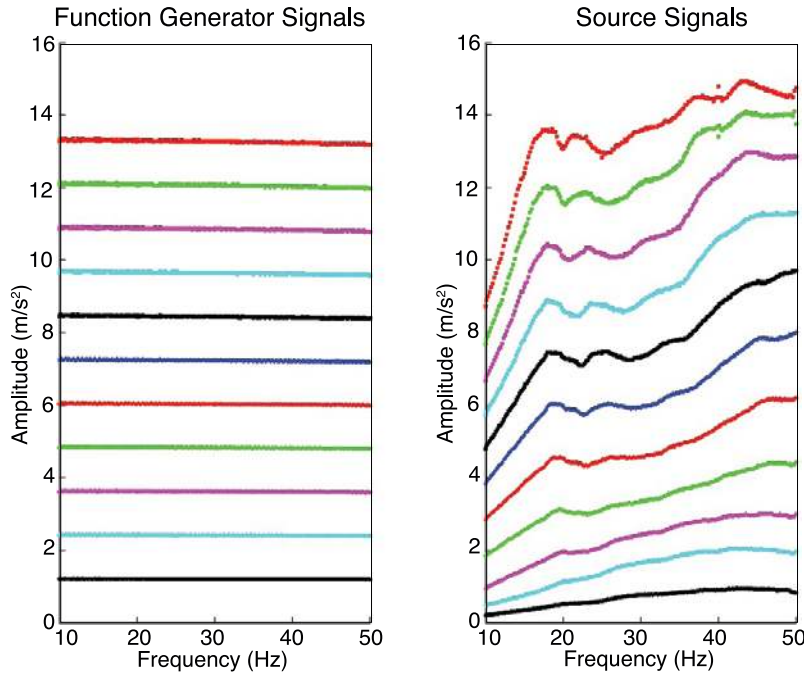
Figure 5. Steady state amplitude spectra measured using the homodyne algorithm for (a) the function generator input and (b) the corresponding (color-coded) measured source output.

first time such an idea has been applied to field data employing a vibrator. We explain the homodyne processing in detail and its relationship to a conventional Fourier spectral analysis in the Appendix.

[19] We estimate the homodyne spectral amplitudes by first dissecting the recorded time signal into a series of time windows. Each window has length $T = Jdt$, with J equal to the number of time samples, At each frequency the truck shook for a duration $\sim 40/f_r$ (a range of 0.8 to 4.0 s) to insure that a steady state response was achieved, although this duration deviated from $40/f_r$ for each frequency because of imprecision in the driving control system. For our analysis we used a short fixed T of 0.8 s for all frequencies and shifted the window, choosing the center of the time window for each frequency so that the homodyne amplitude was maximized at that frequency. The windows may overlap, and were cosine tapered to smooth the edges.

[20] As noted above, at each discrete reference or sweep frequency we window the steady state portion of the receiver signal, u. We denote the reference frequency by f_r, and use it interchangeably with f_m in equation (1). Next we construct two orthonormal, synthetic sine waves with frequency f_r, an in-phase component, $u^I = \sqrt{2/J} \cos(2\pi f_r t)$, and quadrature component $u^Q = \sqrt{2/J} \sin(2\pi f_r t)$. We normalize these so that each has unit energy; that is, considering each as a vector, their dot products are $u^I \bullet u^I = 1$ and $u^Q \bullet u^Q = 1$ where $\bullet$ denotes the vector dot product. The RMS amplitude at a given reference frequency is estimated as

$$R_{n,m} = \sqrt{\frac{2}{J} \left[\left(u \bullet u_m^I \right)^2 + \left(u \bullet u_m^Q \right)^2 \right]} \text{ for } f_m = f_r = f_{\min} \ldots f_{\max}.$$

(8)

$f_{\min}$ and $f_{\max}$ are the minimum and the maximum frequencies of the step sweep (equation (1)). Subscript n refers to the source amplitude (equation (2)). The acceleration signal corresponding to the source-sediment interface is taken through the same procedure resulting in a RMS amplitude vector, $S_{n,m}$. The output from the analysis is a 2-D matrix of RMS amplitudes for each receiver and for the source, with each column referring to a single frequency in the step sweep and each row referring to a source amplitude.

[21] The method provides the means to clearly separate the harmonics from the fundamental target sweep frequencies and is consistent with the input time−frequency protocol. Meaning, for the measured source output, the amplitude at the fundamental sweep frequency is dominant across the entire down sweep.

4.2. Homodyne Results

[22] We compute steady state amplitude spectra for every time signal by extracting the RMS homodyne amplitude at steady state for each discrete frequency in the down sweep. Figure 5 shows the steady state amplitude spectra from the function generator and the measured source output for all source amplitudes. The amplitude spectra for the function generator input are constant across the frequency band, while the amplitude spectra for the measured source output peak near 50 Hz and generally decrease in amplitude as the source frequency decreases. For large source amplitudes, the amplitude spectra have significant structure from 50 Hz down to about 18 Hz and then fall off rapidly. This fall off indicates to us that the truck hydraulics are not producing the signals prescribed by the function generator below $\sim$18 Hz.

[23] The steady state amplitude spectra for all of the receiver components are significantly more complicated than the measured source spectra (Figure 6). At the lowest source amplitude, the receiver spectra are all similar in
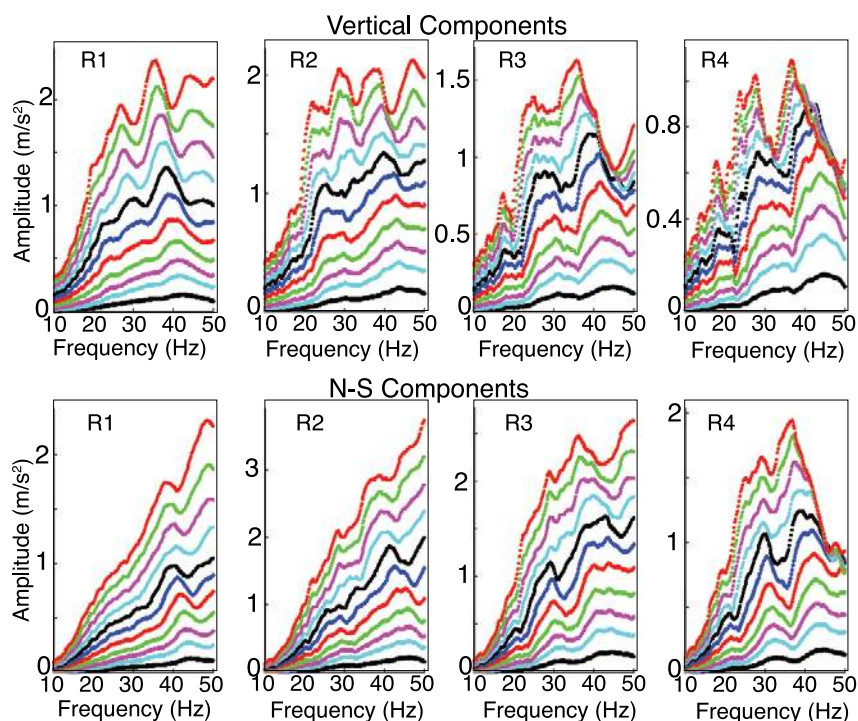
Figure 6. Steady state amplitude spectra measured using the homodyne algorithm for (top) vertical components and (bottom) N–S components recorded at receivers R1, R2, R3, and R4 for function generator and source amplitudes varying as in Figure 7 (same color coding).

structure as opposed to larger source amplitudes where the character of the spectra are more complex and vary depending on receiver location and component. Distinct peaks are observed in the receiver amplitude spectra, particularly for the vertical component, and these peaks appear to shift slightly as the source amplitude increases.

4.3. Spectral Ratios

[24] We compute spectral ratios to analyze the nonlinear soil response, and to separate nonlinearity in the soil column from nonlinearity associated with the source-ground contact region, which we have shown produces significant nonlinearity. As previously noted, spectral ratios are commonly employed to characterize nonlinear behavior in earthquake observations [*Field et al.*, 1997]. The use of spectral ratios relies on a first-order perturbation approximation to the nonlinear system, which introduces some assumptions into our analysis. We assume that the nonlinear behavior of the system is well described by a first-order perturbation of the linear solution (eigenfrequencies/eigenmodes). For our purposes, this assumption is valid for small incremental increases in source amplitude (dA in equation (2)) that result in small changes in the spectral ratios. We must be able to correlate the structure of the spectral ratios for adjacent source amplitudes (A_n to A_{n+1}). If the spectral ratios vary wildly between adjacent source amplitudes, then perturbation theory may not be used to make inferences from the observed shifts in spectral ratios. In addition, using spectral ratios to characterize nonlinear behavior also ignores the coupling between frequencies inherent within nonlinear constitutive relationships. Neglecting the coupling

between frequencies affects the steady state amplitude of the fundamental sweep frequency, producing apparent attenuation because energy is lost to higher-frequency harmonics. However, this loss should not be problematic as long as it does not alter the identification of spectral peaks, since we infer nonlinear-induced material softening from changes in resonance frequencies.

[25] Two types of spectral ratios are computed to characterize the nonlinear behavior of our system. We first compute spectral ratios using the source spectra to normalize receiver spectra. This approach is typically applied in the laboratory to derive the resonance modes of a sample with finite dimensions [*Guyer and Johnson*, 1999; *Johnson*, 1999]. As we expect a combination of standing and propagating modes, and in order to isolate elastic nonlinearity between successive receivers we also compute spectral ratios by dividing adjacent receivers' amplitude spectra. In the following, we present the results for the two spectral ratio methods.
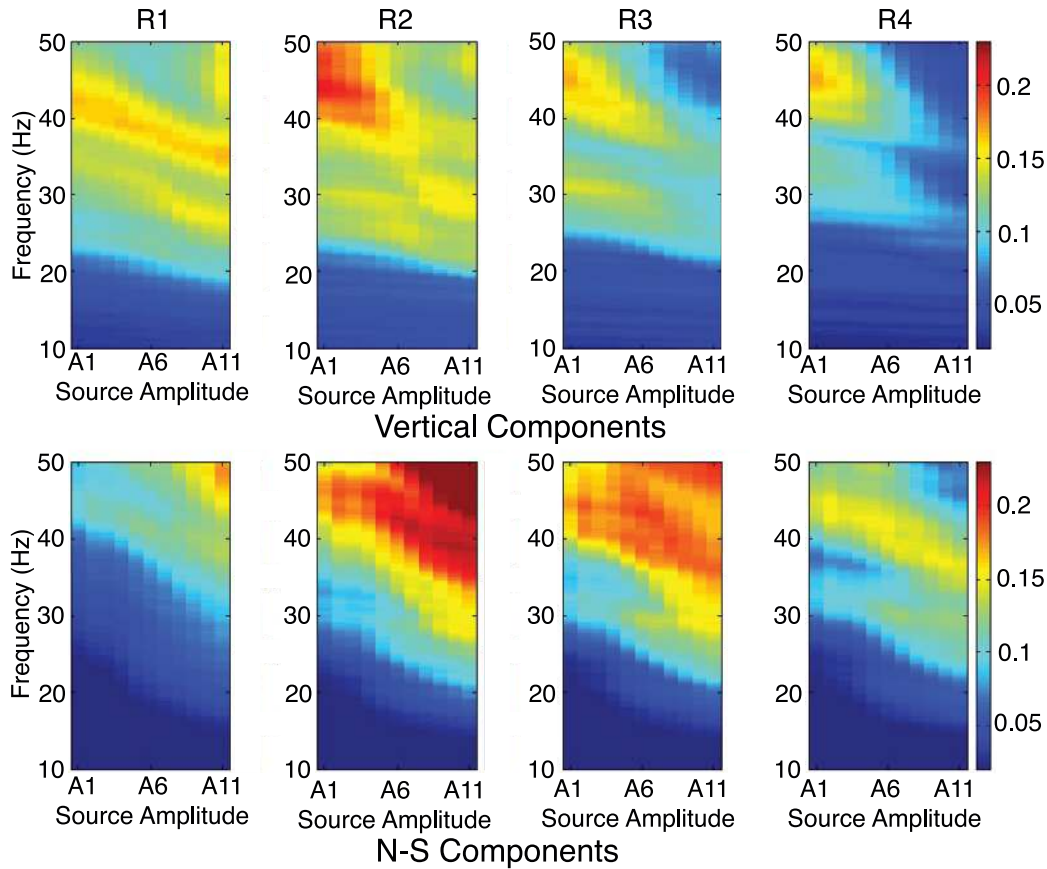
4.3.1. Receiver/Source Ratios

[26] We calculate the spectral ratio, $G(x_i;x_0)$, by dividing the receiver spectra recorded at x_i by the source spectra recorded at x_0 such that

$$G_{n,m}(x_i;x_0) = \frac{R_{n,m}(x_i)}{S_{n,m}(x_0)}. \qquad (9)$$

$G(x_i;x_0)$ is a 2-D matrix with each row corresponding to a source amplitude (A_n), each column corresponding to a fundamental frequency of the down sweep (f_m), and the matrix values corresponding to the spectral ratio amplitudes.

Figure 7. Spectral ratios referenced to the measured source output for (top) vertical components and (bottom) N−S components as a function of source amplitude (*x* axis) for the four receivers R1, R2, R3, and R4. Note that the same color scale is used for all images. Source amplitude increases from left to right.

[27] Figure 7 shows $G(x_i;x_0)$ obtained for the vertical (top) and N−S components (bottom) for R1–R4. As the source amplitude increases, we observe a smooth change in the structure of the spectral ratios. In general, the peak amplitudes of the spectral ratios decrease significantly to lower frequencies as the source amplitude is increased, and this trend is remarkably similar for all receiver components. Although there is considerable complexity, this strongly suggests we have generated and observed significant nonlinearity in the form of resonant frequency shifts associated with modulus softening as a function of drive amplitude.

[28] The spectral ratios all show a significant decrease in amplitude below about 20 Hz, where the truck did not operate well perhaps because of impaired ground coupling of the vibrator base plate. It is known that the T-Rex does not operate well below 10 Hz, but the data suggest that below about 20 Hz in our experiment it became unstable, producing more harmonics and smaller ground forcing. This behavior is also seen in Figures 5 and 6.

4.3.2. Receiver/Receiver Ratios

[29] Above, we isolated the nonlinear response between each successive receiver and the source. In order to reduce any contamination from potential nonlinear coupling of the vibrator plate to the ground we further isolate the elastic nonlinearity between receiver pairs. We define the spectral ratio between adjacent receiver pairs as

$$G_{n,m}(x_i;x_j) = \frac{R_{n,m}(x_i)}{R_{n,m}(x_j)}. \qquad (10)$$

$G_{n,m}(x_i;x_j)$ should measure the response of the sediment column, and the associated nonlinearity. Figure 8 shows $G_{n,m}(x_i;x_j)$ derived for vertical components and N−S components. In contrast to the receiver/source $G(x_i;x_0)$ shown in the Figure 7, the peaks in $G_{n,m}(x_i;x_j)$ show decreases in frequency that begin relatively flat and then decrease rapidly for the larger source amplitudes. This is similar in shape and behavior to modulus reduction curves ($\mu_{effective}/\mu_{max}$ versus strain) found in geotechnical literature. In addition, the peaks are much sharper (narrower in frequency), and significant structure is observed throughout the frequency band. The large amplitude N/S peak in the R2/R1 ratio, for example, decreases in frequency from ∼37.5 Hz to ∼28 Hz, about 75% of its unshaken value. These ratios, in contrast to the receiver/source ratios, span a much larger amplification range (e.g., the largest range is from 1.2 to 2.2 amplification for the R2/R1 N−S
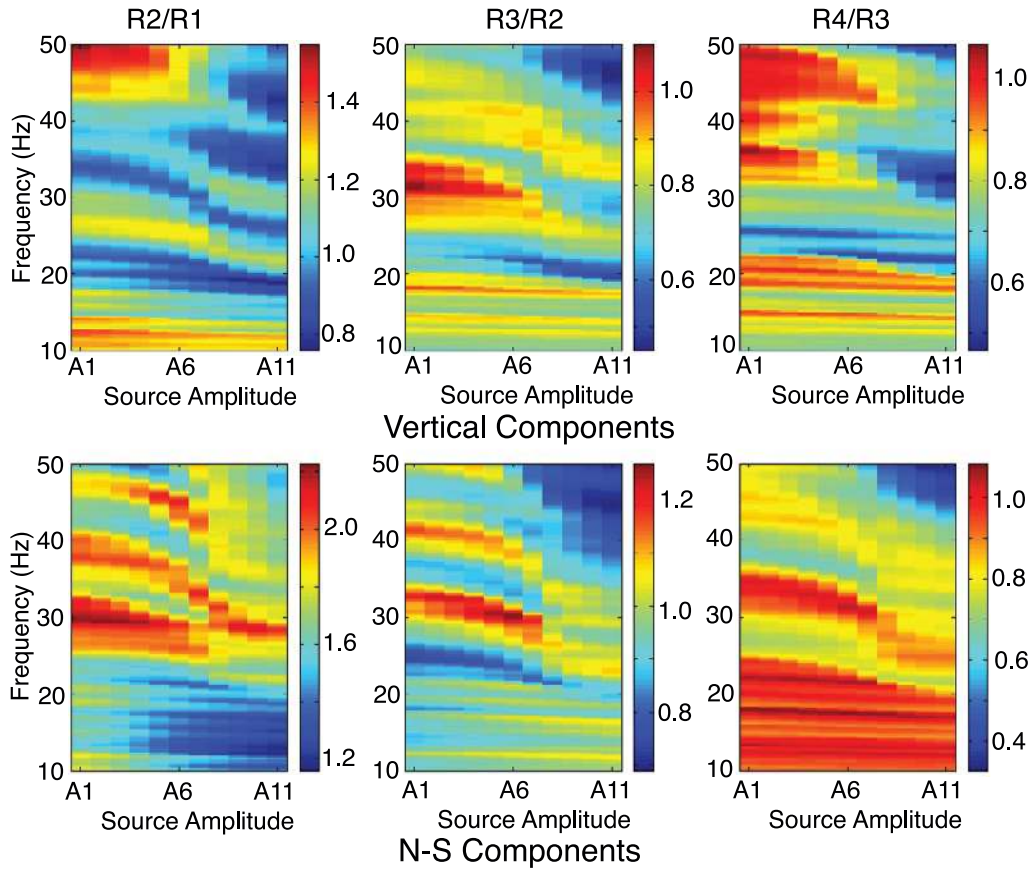
Figure 8. Spectral ratios computed for (top) vertical components and (bottom) N−S components using adjacent station pairs R2/R1, R3/R2, and R4/R3. Note that each image has a different color scale. Source amplitude increases from left to right.

components ratio) implying relative amplification between stations, suggestive of strong reverberations within layers. These apparently dominate any damping with distance.

5. Discussion

[30] Our experiments reveal in situ bulk and shear modulus reduction induced by a large vibrator truck. The bulk and shear modulus reductions are manifest as changes in the frequencies of site resonances that show up as peaks in the homodyne-derived spectra and spectral ratios. In the case of shear, assuming that the resonance peaks result from trapped horizontal shear waves, at least for the sensors closest to the source, then the frequency of the resonance peak, f_r, is expected to be related to the shear wave velocity, V_s, of the resonant layer of thickness, H, by

$$V_s = 4Hf_r. \tag{11}$$

The shear wave velocity is related to the shear modulus, μ, and density, ρ, by

$$V_s = \sqrt{\mu/\rho}. \tag{12}$$

If the density and resonant layer thickness do not change, then the observed frequency reduction will be the square root of the corresponding modulus reduction. In the example from section 4.3.2 this implies a modulus reduction to about 56% of its unforced value.

[31] We comment briefly on differences between the responses of horizontal and vertical components of the wavefield, noting that field observations from natural earthquakes suggest that nonlinearity is stronger in response to horizontal motions than vertical ones [e.g., see *Bonilla et al.*, 2005]. Laboratory studies of glass beads under bulk mode and shear mode resonance support this observation (X. Jia, personal communication, 2008). From Figure 8 we can infer qualitative comparison. For instance, comparing the ratio R2/R1 for the vertical and N−S components, the prominent peak at 26 Hz in the vertical ratio shifts by about 5 Hz, corresponding to a modulus reduction to about 65% of its unforced value, a smaller modulus reduction than we estimate above for the horizontal components.

[32] The modulus reductions we estimate in this experiment at the Capital Aggregates site near Austin, Texas are consistent with data analyses presented by *Lawrence et al.* [2008, 2009], which describe experiments at different sites (in California and Arkansas, respectively) that employed the same, or a similar, vibrator truck as we used in this study. Those experiments focused on the analyses of surface waves produced by the vibrator truck, and modulus reductions were revealed as changes in dispersion curves and verified by phase moveouts across the array. Modulus

reductions in the range of 55% to 65% of the unreduced value were found for strains estimated by *Lawrence et al.* [2008] from the wavefield to be approximately 4×10^{-4} to 1.5×10^{-4}, although the uncertainties were very large. Laboratory measurements of shear modulus reduction from resonant column testing of material taken from the site we investigated in this experiment reveal modulus reductions of that range at shear strains of about 4×10^{-4} to 2×10^{-4} [*Kurtulus et al.*, 2005]. The values we estimate in this study are made in situ, may be found from a single station pair, and presume a different wave model consisting dominantly of trapped resonant body waves.

[33] The wavefield in the near field of the vibrating source may be quite complex in general, with contributions from reverberating body waves trapped in layers, and the associated surface waves generated from their constructive interference. Challenges to modeling the wavefield may result from the finite source dimensions and changes to the soil structure arising from the induced nonlinear behavior itself. Our present study shows that a complete understanding of the wavefield is not necessary to characterize nonlinear modulus reduction. The simplest view, that of a field analog to laboratory resonant column testing, yields similar results. We note theoretical results by *Xu et al.* [2006] suggesting that layer reverberations may dominate the wavefield within several meters of the source given the Capital Aggregates test site soil structure.

[34] Both standing waves and surface waves are more sensitive to deeper structure as their frequencies decrease and wavelengths correspondingly increase. At the same time, overburden increases with depth, the nonlinearity is diminished, as is born out in numerous laboratory studies [*Hardin and Drnevich*, 1972; *Johnson and Jia*, 2005; *Zinszner et al.*, 1997]. Full-scale, nonlinear modeling will be required to quantitatively assess the relationship between frequency and depth. Recently, nonlinear wave propagation codes have been developed that incorporate laboratory derived soil properties into predictions of nonlinear site response [*Bonilla et al.*, 2005]; however, these nonlinear wave propagation models rely on a simple hysteretic soil model. such as the extended Masing's rules, are limited to 1-D shear wave propagation, and do not incorporate more complex phenomena such as harmonic generation and nonlinear surface waves. Observations such as those presented herein may ultimately permit the development of more rigorous numerical models of nonlinear soil behavior under natural conditions, not possible using laboratory data alone.

6. Conclusions

[35] In this study, we describe a novel approach for study of in situ, nonlinear site response using a vibrator truck and new processing methods. The methodology was applied to a natural soil site and provided noninvasive measurements of the nonlinear soil behavior at wavelengths and amplitudes similar to those of actual earthquakes, although lower-frequency information will be key to a more complete site response study. We obtain a detailed, semiquantitative picture of the nonlinear soil response by taking measurements at progressively increasing excitation levels. Careful analysis using a homodyne algorithm developed here and applied for the first time on field seismological data, and

spectra ratios of signals measured at the source and an array of seismometers, provided the means for minimizing the contribution of harmonics and the separation of source-generated nonlinearity from pervasive nonlinearity in the sediment column.

[36] We believe that such in situ dynamic testing has the potential to contribute to the understanding of elastic nonlinear behavior of undisturbed soils and thus to validate the accuracy of nonlinear soil models. Ultimately, such observations should lead to a better theoretical understanding of nonlinear wave propagation, which is critical to the development of inverse methods for extracting nonlinear soil parameters from field-scale measurements and perhaps more importantly, for predicting nonlinear response in regions where no measurements from natural earthquakes exist or are likely in the near future. Similar experiments should be conducted at sites where previous nonlinear site response has been observed in order to further validate the methodology and should attempt to employ an active source with more controllable power at even lower frequencies.

Appendix A

[37] Here we describe the details of the homodyne analysis. Our goal in this study was to measure for each sweep or reference angular frequency, ω_r, the amplitude of the ground response at the same frequency. Homodyne processing is commonly used in situations where the system response is to be measured at specific frequencies emitted by a known source. For example, laboratory experiments often use a lock-in amplifier, which employs a homodyne, to conduct real-time measurements of receiver amplitudes at a single frequency of a controlled source. In this study, we also have a controlled source (the vibrator truck) and wish to measure the amplitude at many specific source (sweep) frequencies. Therefore, the analysis of our experiment's data lends itself to homodyne processing, albeit after the data has been collected.

[38] The advantages of the homodyne are that it is simple to implement and only requires the computation of Fourier coefficients at a specified frequency, independently of those not of interest. In this sense, it effectively simultaneously filters the data in a narrow band around the frequency of interest and provides an accurate measure of the Fourier amplitude and phase at that frequency. While a conventional discrete Fourier transform (FFT) based approach could also be employed, it would not provide amplitudes at the exact source frequencies we prescribed (FFT frequencies being fixed by the record length), and would also output amplitudes at many other frequencies that are not of interest. For these reasons, we chose to use the homodyne to analyze the field data from our experiment.

A1. Discrete or Fast Fourier Transform

[39] The goal of the homodyne analysis is to extract the amplitude of the frequency component of a specified reference frequency, ω_r, from an observed signal, $u(t)$, that contains multiple frequency components. Here we show that the spectral amplitude of a single frequency component of an FFT is equivalent to that estimated using the homodyne processing. The differences however, are that for the FFT the precise frequencies, ω_n, are determined by the record length, T, and sampling interval. Additionally the FFT solves

for all frequency component amplitudes and phases simultaneously. In an FFT the frequency components, $U(\omega_n)$, are estimated by forming the sum

$$U(\omega_n) = \sum_{j=1}^{J} u(t_j)e^{i\omega_n t_j}$$
$$= \sum_{j=1}^{J} u(t_j)\cos(\omega_n t) + i\sum_{j=1}^{J} u(t_j)\sin(\omega_n t)$$
$$= u \bullet u^I + iu \bullet u^Q. \tag{A1}$$

As in the main text, we write in-phase and quadrature component synthetic sine waves as vectors, with jth elements $u^I = \sqrt{2/J}\cos(\omega_r t_j)$ and $u^Q = \sqrt{2/J}\sin(\omega_r t_j)$, and the dot indicates a dot product of these with the data vector. We choose this normalization so that these sine waves have unit energy (i.e., the dot product with itself is unity). Thus, comparing the FFT represented by equation (A1) to the homodyne (equation (8) in the text)

$$\overline{A} = \sqrt{\frac{2}{J}\left[(u \bullet u^I)^2 + (u \bullet u^Q)^2\right]}, \tag{A2}$$

we see that the spectral amplitude of a single frequency component of an FFT is equivalent to that estimated using the homodyne processing when $\omega_r = \omega_n$. In both the FFT and the homodyne there are considerations of resolution and accuracy that arise because of the finite record length, discrete sampling, and noise characteristics. We note some of these in the following discussion of the homodyne.

A2. Homodyne

[40] The general concept of the homodyne is as follows. A detected signal is multiplied by a pure sine wave at a reference frequency, ω_r (any frequency of interest). Because sine waves of differing frequencies are orthogonal (i.e., the average of the product of two sine waves of different frequencies is zero) the result of multiplying the detected signal and the sine wave with the reference frequency yields a DC output signal proportional to the amplitude of the frequency component of the detected signal at the frequency of the reference sine wave. In other words, the output product is locked to the reference frequency. As with an FFT and as we show below for the homodyne, we cannot measure a frequency component perfectly because we have only a finite record length.

[41] More explicitly, the homodyne is a time domain analysis that takes advantage of the orthonormal properties of sine waves and requires the summation over time points implicit in the FFT (equation (A1)) but only for the frequency of interest. We show that this works effectively by considering our observed signal as a superposition of sine waves at all frequencies. Each component sine wave of $u(t)$ can be written as

$$U(\omega,t) = A(\omega)\sin[\omega t + \varphi(\omega)]$$
$$= c(\omega)\cos\varphi\sin(\omega t) + d(\omega)\sin\varphi\cos(\omega t)$$
$$= C(\omega)\sin(\omega t) + D(\omega)\cos(\omega t)$$
$$A(\omega)^2 = C(\omega)^2 + D(\omega)^2$$
$$\varphi(\omega) = \tan^{-1}[C(\omega)/D(\omega)]. \tag{A3}$$

[42] A and φ describe the amplitude and initial phase of the signal, respectively, and ω is angular frequency. Note

that in the equations that follow we have sometimes omitted the frequency-dependence of the terms, $C(\omega)$ and $D(\omega)$, in equation (A3) for notational simplicity only.

[43] For those interested only in the answer, we state the explicit result of the homodyne (equation (A2)) now and follow with the detailed derivation. The former can be written as

$$u \bullet u^I \sim -\sqrt{T/2}\{D(\omega_r) + \text{sinc}(\omega_r T)$$
$$\cdot [C(\omega_r)\sin(2\omega_r t_c) + D(\omega_r)\cos(2\omega_r t_c)]\}$$
$$u \bullet u^Q \sim -\sqrt{T/2}\{C(\omega_r) + \text{sinc}(\omega_r T)$$
$$\cdot [-C(\omega_r)\cos(2\omega_r t_c) + D(\omega_r)\sin(2\omega_r t_c)]\}. \tag{A4}$$

[44] If we can neglect the terms multiplied by the sinc function and substitute this into the expression for the homodyne (equation (A2)) we recover the spectral amplitude at ω_r exactly (i.e., $A(\omega_r)$ in equation (A3)). (The homodyne and discrete FFT (equations (A1) and (A2)) do not account for the sample interval, dt, so that in them J is used instead of T, which equals Jdt.) $\text{sinc}(\omega_r T)$ becomes negligibly small if we choose T sufficiently long relative to ω_r^{-1}. Explicitly, this requires that $T \gg \pi/\omega_r$ or $T\omega_r/2\pi \gg 1/2$. In our experiment we vibrated at each sweep frequency long enough that $T\omega_r/2\pi \sim 40$, which corresponds to T equal to 0.8 to 4.0 s for the sweep range of 50 to 10 Hz, respectively. However, for the homodyne estimates at all frequencies we use a fixed window of $T = 0.8$ s (see text), but this still insures the condition for an accurate solution is satisfied (i.e., the minimum value of $T\omega_r/2\pi = 8$ at 10 Hz). In short, the homodyne processing effectively isolates the frequency component of interest (i.e., eliminates all other components) and ensures an accurate measure of its amplitude and phase.

[45] To derive the result expressed as equation (A4) we first consider the product of a single frequency component of the observed signal with a pure cosine or "in-phase" wave at reference frequency, $u^I = \sqrt{2/T}\cos(\omega_r t)$. The result is

$$U(\omega,t) \times u^I = U(\omega,t) \times \sqrt{2/T}\cos(\omega_r t)$$
$$= \sqrt{2/T}\{C\sin(\omega t)\cos(\omega_r t) + D\cos(\omega t)\cos(\omega_r t)\}$$
$$= 1/2\sqrt{2/T}\{C[\sin(\Delta_- t) + \sin(\Delta_+ t)] + D$$
$$\cdot [\cos(\Delta_- t) + \cos(\Delta_+ t)]\}. \tag{A5a}$$

Similarly, the product with the "quadrature" (90° initial phase) sine wave, $u^Q = \sin(\omega_r t)$, is

$$U(\omega,t) \times u^Q = U(\omega,t)\sqrt{2/T}\sin(\omega_r t)$$
$$= \sqrt{2/T}\{C\sin(\omega t) + \sin(\omega_r t) + D\cos(\omega t)\sin(\omega_r t)\}$$
$$= 1/2\sqrt{2/T}\{C[\cos(\Delta_- t) - \cos(\Delta_+ t)] + D$$
$$\cdot [-\sin(\Delta_- t) + \sin(\Delta_+ t)]\}. \tag{A5b}$$

These equations apply to all time points (subscripts omitted for simplicity). We define the difference and summed frequencies, $\Delta_- = (\omega - \omega_r)$ and $\Delta_+ = (\omega + \omega_r)$, and have used the basic trigonometric identities

$$2 \sin(\omega t) \cos(\omega_r t) = \sin(\Delta_- t) + \sin(\Delta_+ t)$$
$$2 \cos(\omega t) \sin(\omega_r t) = -\sin(\Delta_- t) + \sin(\Delta_+ t)$$
$$2 \cos(\omega t) \cos(\omega_r t) = \cos(\Delta_- t) + \cos(\Delta_+ t)$$
$$2 \sin(\omega t) \sin(\omega_r t) = \cos(\Delta_- t) - \cos(\Delta_+ t) \qquad (A6)$$

Now we can write the summation over all time points, t_j for $j = 1, \ldots J$, or equivalently the inner or dot products of u with u^I or u^Q (these now refer to vectors). Again, for a single frequency component of u, these can be written

$$U \bullet u^I = \sqrt{2/T} \, \{\frac{C}{2} \sum_{j=1}^{J} \left[\sin(\Delta_- t_j) + \sin(\Delta_+ t_j) \right] + \frac{D}{2} \sum_{j=1}^{J}$$
$$\cdot \left[\cos(\Delta_- t_j) + \cos(\Delta_+ t_j) \right] \}$$
$$U \bullet u^Q = \sqrt{2/T} \, \{\frac{C}{2} \sum_{j=1}^{J} \left[\cos(\Delta_- t_j) - \cos(\Delta_+ t_j) \right] + \frac{D}{2} \sum_{j=1}^{J}$$
$$\cdot \left[-\sin(\Delta_- t_j) + \sin(\Delta_+ t_j) \right] \} \qquad (A7)$$

We can eliminate the summations in equation (A7) to obtain a closed-form expression if we consider the time series to be continuous and substitute the summations with integrals. As an example we show the details of evaluating the first summation of $U \bullet u^I$ as an integral, as follows

$$\sum_{j=1}^{J} \sin(\Delta_- t_j) \approx \int_{t_c - T/2}^{t_c + T/2} \sin(\Delta_- t) dt$$
$$= \frac{1}{\Delta_-} \left\{ \cos\left[\Delta_- \left(t_c + T/2 \right) \right] - \cos\left[\Delta_- \left(t_c - T/2 \right) \right] \right\}$$
$$= -\frac{2}{\Delta_-} \sin\left(\frac{\Delta_- T}{2} \right) \sin(\Delta_- t_c)$$
$$= -T \frac{\sin\left(\frac{\Delta_- T}{2} \right)}{\left(\frac{\Delta_- T}{2} \right)} \sin(\Delta_- t_c)$$
$$= -T \mathrm{sinc}\left(\frac{\Delta_- T}{2} \right) \sin(\Delta_- t_c) \qquad (A8)$$

t_c is the center of the time window, or $(t_j + t_1)/2$. Similar expressions are obtained for all the other terms, and all have sinc functions with arguments $\Delta_- T/2$ or $\Delta_+ T/2$. Thus, the equivalent expression to equation (A7) can be written as

$$U \bullet u^I = -\sqrt{T/2} \, \{\mathrm{sinc}\left(\frac{\Delta_- T}{2} \right)$$
$$\cdot \left[C(\omega) \sin(\Delta_- t_c) + D(\omega) \cos(\Delta_- t_c) \right]$$
$$+ \mathrm{sinc}\left(\frac{\Delta_+ T}{2} \right) \left[C(\omega) \sin(\Delta_+ t_c) + D(\omega) \cos(\Delta_+ t_c) \right] \}$$
$$U \bullet u^Q = -\sqrt{T/2} \, \{\mathrm{sinc}\left(\frac{\Delta_- T}{2} \right)$$
$$\cdot \left[C(\omega) \cos(\Delta_- t_c) - D(\omega) \sin(\Delta_- t_c) \right]$$
$$+ \mathrm{sinc}\left(\frac{\Delta_+ T}{2} \right) \left[-C(\omega) \cos(\Delta_+ t_c) \right.$$
$$\left. + D(\omega) \sin(\Delta_+ t_c) \right] \}. \qquad (A9)$$

Equation (A9) shows that the quantities we seek to measure, $C(\omega)$ and $D(\omega)$, are multiplied by sinc functions with arguments that depend on $\Delta_- = (\omega - \omega_r)$ and $\Delta_+ = (\omega + \omega_r)$. The properties of sinc functions effectively isolate the frequency of interest, $\omega = \omega_r$; that is, they act as filters to eliminate the signal at other frequencies. To see this note that when $\omega \sim \omega_r$, $\Delta_- \sim 0$, and $\Delta_+ \sim 2\omega_r$ and equations (A4) result, which summarize the essence of the homodyne. Because only the ω_r frequency component of u contributes to the result we can substitute U in equation (A9) with u in equation (A4).

[46] The validity of the approximation made going from equations (A9) to (A4), or the extent to which energy from other frequency components is not eliminated (i.e., the resolution) is determined by the window length and is approximately $(\omega - \omega_r) \sim 2\pi/T$ (the first zero in the sinc function). For the value of $T = 0.8$ s we use, this corresponds to a frequency resolution of ~ 0.625 Hz.

References

Beresnev, I. A., and K. L. Wen (1996), Nonlinear soil response—A reality?, *Bull. Seismol. Soc. Am.*, 86, 1964–1978.

Bonilla, L. F., J. H. Steidl, J.-C. Gariel, and R. J. Archuleta (2002), Borehole response studies at the Garner Valley downhole array, southern California, *Bull. Seismol. Soc. Am.*, 92, 3165–3179, doi:10.1785/0120010235.

Bonilla, L. F., R. J. Archuleta, and D. Lavallée (2005), Hysteretic and dilatant behavior of cohesionless soils and their effects on nonlinear site response: Field data observations and modeling, *Bull. Seismol. Soc. Am.*, 95, 2373–2395, doi:10.1785/0120040128.

Brunet, T., X. Jia, and P. A. Johnson (2008), Transitional nonlinear elastic behaviour in dense granular media, *Geophys. Res. Lett.*, 35, L19308, doi:10.1029/2008GL035264.

Darendeli, M. B. (2001), Development of a new family of normalized modulus reduction and material damping curves, Ph.D. dissertation, 362 pp., Univ. of Tex. at Austin, Austin.

Field, E. H., P. A. Johnson, I. Beresnev, and Y. Zeng (1997), Nonlinear ground-motion amplification by sediments during the 1994 Northridge earthquake, *Nature*, 390, 599–602, doi:10.1038/37586.

Field, E. H., Y. Zeng, P. A. Johnson, and I. A. Beresnev (1998), Nonlinear sediment response during the 1994 Northridge earthquake: Observations and finite source simulations, *J. Geophys. Res.*, 103, 26,869–26,883, doi:10.1029/98JB02235.

Guyer, R. A., and P. A. Johnson (1999), Nonlinear mesoscopic elasticity: Evidence for a new class of materials, *Phys. Today*, 52, 30–35, doi:10.1063/1.882648.

Hardin, B. O. (1972), Shear modulus and damping in soils: Design equations and curves, *J. Soil Mech. Found. Div. Am. Soc. Civ. Eng.*, 98, 667–692.

Hardin, B. O., and V. P. Drnevich (1972), Shear modulus and damping in soils: Measurement and parameter effects, *J. Soil Mech. Found. Div. Am. Soc. Civ. Eng.*, 98, 603–624.

Holzer, T. L., and T. L. Youd (2007), Liquefaction, ground oscillation, and soil deformation at the Wildlife Array, California, *Bull. Seismol. Soc. Am.*, 97, 961–976, doi:10.1785/0120060156.

Holzer, T. L., T. C. Hanks, and T. L. Youd (1989), Dynamics of liquefaction during the 1987 Superstition Hills, California, earthquake, *Science*, 244, 56–59, doi:10.1126/science.244.4900.56.

Johnson, P. (1999), The new wave in acoustic testing, *Mater. World*, 7, 544–546.

Johnson, P. A., and X. Jia (2005), Nonlinear dynamics, granular media and dynamic earthquake triggering, *Nature*, 437, 871–874, doi:10.1038/nature04015.

Johnson, P. A., and A. Sutin (2005), Slow dynamics and anomalous fast dynamics in diverse solids, *J. Acoust. Soc. Am.*, 117, 124–130, doi:10.1121/1.1823351.

Johnson, P. A., B. Zinszner, and P. N. J. Rasolofosaon (1996), Resonance and elastic nonlinear phenomena in rock, *J. Geophys. Res.*, *101*, 11,553–11,564, doi:10.1029/96JB00647.

Kurtulus, A., J. J. Lee, and K. H. Stokoe (2005), Summary report: Site characterization of Capital Aggregates test site, internal report, 47 pp., Univ. of Tex. at Austin, Austin.

Lawrence, Z., P. Bodin, C. A. Langston, F. Pearce, J. Gomberg, P. A. Johnson, F. Y. Menq, and T. Brackman (2008), Induced dynamic nonlinear ground response at Garner Valley, California, *Bull. Seismol. Soc. Am.*, *98*, 1412–1428, doi:10.1785/0120070124.

Lawrence, Z., P. Bodin, and C. A. Langston (2009), In situ measurements of nonlinear and nonequilibrium dynamics in shallow, unconsolidated sediments, *Bull. Seismol. Soc. Am.*, in press.

Lebedev, A. V., and I. A. Beresnev (2004), Nonlinear distortion of signals radiated by vibroseis sources, *Geophysics*, *69*, 968–977, doi:10.1190/1.1778240.

Lebedev, A. V., I. A. Beresnev, and P. L. Vermeer (2006), Model parameters of the nonlinear stiffness of the vibrator-ground contact determined by inversion of vibrator accelerometer data, *Geophysics*, *71*, H25–H32.

Loukachev, I., N. Pralle, and G. Gudehus (2002), Dilatancy-induced *P* waves as evidence for nonlinear soil behavior, *Bull. Seismol. Soc. Am.*, *92*, 854–862, doi:10.1785/0120010115.

Pavlenko, O. V., and K. Irikura (2003), Estimation of nonlinear time-dependent soil behavior in strong ground motion based on vertical array data, *Pure Appl. Geophys.*, *160*, 2365–2379, doi:10.1007/s00024-003-2398-9.

Satoh, T., T. Sato, and H. Kawase (1995), Nonlinear behavior of soil sediments identified by using borehole records observed at the Ashigra Valley, Japan, *Bull. Seismol. Soc. Am.*, *85*, 1821–1834.

Satoh, T., M. Fushimi, and Y. Tatsumi (2001), Inversion of strain-dependent nonlinear characteristics of soils using weak and strong motions observed by borehole sites in Japan, *Bull. Seismol. Soc. Am.*, *91*, 365–380, doi:10.1785/0120000049.

Seed, H. B., R. T. Wong, I. M. Idriss, and K. Tokimatsu (1986), Moduli and damping factors for dynamic analyses of cohesionless soils, *J. Geotech. Eng.*, *112*, 1016–1032, doi:10.1061/(ASCE)0733-9410(1986)112:11(1016).

Steidl, J. H., A. G. Tumarkin, and R. J. Archuleta (1996), What is a reference site?, *Bull. Seismol. Soc. Am.*, *86*, 1733–1748.

Stokoe, K. H., P. J. Axtell, and E. M. Rathje (2001), Development of an in situ method to measure nonlinear soil behavior, in *Earthquake Resistant Engineering Structures III*, *Adv. Earthquake Eng.*, vol. 9, edited by C. A. Brebbia and A. Corz, pp. 561–570, WIT, Southampton, U. K.

TenCate, J. A., and T. J. Shankland (1996), Slow dynamics in the nonlinear elastic response of Berea sandstone, *Geophys. Res. Lett.*, *23*, 3019–3022, doi:10.1029/96GL02884.

Van Den Abeele, K. E.-A., J. Carmeliet, P. A. Johnson, and B. Zinszner (2002), Influence of water saturation on the nonlinear elastic mesoscopic response in Earth materials and the implications to the mechanisms of nonlinearity, *J. Geophys. Res.*, *107*(B6), 2121, doi:10.1029/2001JB000368.

Williams, R. A., W. J. Stephenson, A. D. Frankel, E. Cranswick, M. E. Meremonte, and J. K. Odum (2000), Correlation of 1- to 10-Hz earthquake resonances with surface measurements of *S*-wave reflections and refractions in the upper 50 m, *Bull. Seismol. Soc. Am.*, *90*, 1323–1331, doi:10.1785/0120000009.

Xu, Y., J. Xia, and R. D. Miller (2006), Quantitative estimation of minimum offset for multichannel surface-wave survey with actively exciting source, *J. Appl. Geophys.*, *59*, 117–125, doi:10.1016/j.jappgeo.2005.08.002.

Zinszner, B., P. A. Johnson, and P. N. J. Rasolofosaon (1997), Influence of change in physical state on elastic nonlinear response in rock: Significance of effective pressure and water saturation, *J. Geophys. Res.*, *102*, 8105–8120, doi:10.1029/96JB03225.

———————————

P. Bodin, Department of Earth and Space Sciences, University of Washington, Box 381310, Seattle, WA 98195-1310, USA.

J. Gomberg, U.S. Geological Survey, Department of Earth and Space Sciences, University of Washington, Box 381310, Seattle, WA 98195-1310, USA. (gomberg@usgs.gov)

P. Johnson, Geophysics Group, Los Alamos National Laboratory, Mail Stop D443, Los Alamos, NM 87545, USA. (paj@lanl.gov)

Z. Lawrence, ExxonMobil Upstream Research Company, Houston, TX 77252-2189, USA.

F.-Y. Menq, Geotechnical Engineering Center, Department of Civil, Architectural and Environmental Engineering, University of Texas at Austin, 9.227 Ernest Cockrell Jr. Hall, 301 East Dean Keeton Street, Austin, TX 78712, USA.

F. Pearce, Earth Resources Laboratory, MIT, Boston, MA 02139, USA.